WILEY | Hindawi

Research Article

Evolutions of Anisotropic Hydraulic Properties of Rough-Walled Rock Fractures under Different Shear Displacements

Dapeng Lu [ID]

China Railway No. 10 Engineering Group Co. Ltd., Jinan 250101, China

Correspondence should be addressed to Dapeng Lu; dapenglu@126.com

Four cylindrical sandstone samples were extracted from the original rectangular sample with a rough-walled fracture. Each drilling angle (θ) of cylindrical sandstone samples is different to consider the anisotropies of rough-walled rock fractures. For each sample, different flow velocities ranging from 0 m/s to 13 m/s were designed. For a given flow velocity, a series of different confining pressures (σ_n), including 1.5 MPa, 2.5 MPa, and 3.5 MPa, were applied on the fractured samples. The hydraulic properties of each cylindrical sandstone sample were tested under different shear displacements (u_s) and σ_n. The results show that the hydraulic gradient (J) shows an increasing trend with the increment of σ_n. With the increment of the Reynolds number (Re), the transmissivity (T) decreases in the form of the quadratic function. The normalized transmissivity (T/T_0) decreases with the increment of J. The variations in T/T_0 with J can be divided into three stages. The first stage is that T/T_0 approximately holds a constant value of 1.0 when J is small indicating that the fluid flow is in the linear regime. The last two stages are that T/T_0 decreases with the continuous increase of J, and the reduction rate first increases and then decreases. The critical Reynolds' number (Re_c) of the sample angle with a drilling angle of 90° is different from that of other samples. The corresponding Re_c is 6.52, 28.73, and 32.1 when the shear displacement (u_s) = 2 mm, 3 mm, and 4 mm, respectively. The variations in Re_c and J along different drilling angles are significantly obvious. When the confining pressure is large, the effect of anisotropy on Re_c is much greater than that of confining pressure.

1. Introduction

Rock fracture network plays a critical role in controlling the main paths of contaminant migration and fluid flow in tight rock masses [1–5]. During the past several decades, the permeability of fractured rock masses has been extensively studied in many geosciences and geoengineering such as geothermal energy development, enhanced oil recovery, and CO_2 sequestration [6, 7]. The rock fractures are commonly assumed to be parallel plate models and obey the cubic law, in which the flow rate is linearly correlated to the hydraulic gradient [3, 8]. However, the natural surface of fractures is rough, in which fluid flows through the nonlinear flow regime, and the flow rate is nonlinearly proportional to the hydraulic gradient [9]. Therefore, the estimation of the hydraulic properties of rough-walled rock fractures contributes to the accurate assessment of the flow properties of fractured rock masses.

Previous studies have reported that the geometry of rough-walled fractures significantly influences the flow properties of the rock masses [2, 10–14]. Zou et al. [14] developed a two-dimensional (2D) finite volume method (FVM) code to examine the effects of the original wall surface roughness of fractures on fluid flow. Liu et al. [2] summarized the mathematical expressions for the effects of aperture distribution and anisotropy on the equivalent permeability of DFNs. Huang et al. [11] originally developed a numerical procedure to effectively calculate fluid flow through 3D discrete fracture network (DFN) models and systematically investigated the roughness of fracture surface and anisotropy of aperture distribution on the permeability of DFN models. Kong and Chen [12] simulated fluid flow behavior within the three-dimensional (3D) rough fractures to study the influence of the properties of the rough fracture surface on the fracture conductivity. He et al. [10] carried out laboratory triaxial seepage tests to study the seepage characteristics of the columnar

fractured rock masses at the Baihetan hydropower dam sites. The experimental results showed that the similar material model samples of columnar fractured rock mass showed obvious seepage anisotropies. Gong et al. [15, 16] presented a new heavily parallelized, dynamic pore-network modeling platform that is capable of simulating two-phase flow in rough-walled fractures with high computational efficiency. Lavrov [13] performed four finite-difference schemes to numerically evaluate the fluid flow in rough-walled fractures. However, underground excavation and/or earthquakes can induce significant deformation of preexisting fractures in rock masses. Due to the slip-along fractures, the flow properties of fractured rock masses can be influenced. Therefore, considering the effect of shear displacement on the flow properties of fractured rock masses is necessary.

Many studies have focused on the effect of share-induced deformation [17–24]. Kim et al. [24] developed analytical and numerical techniques, which combined micromechanics-based continuum (MBC) model analysis and FracMan/Mafic package, for calculating fluid flow through a single rock joint and the transmissivities due to shearing. Ahmadi et al. [17] imposed contact asperities of saw-tooth-like structures and in the shear direction to investigate the effects of the degree of contact between the fracture faces on the compliance ratio in the stiff direction. Lang et al. [20] developed a numerical approach to investigate the influences of transmissivity anisotropy induced by shearing on the overall permeability of fractured rock masses based on contact mechanics. Liu et al. [21, 22] proposed a modified successive random additions (SRA) algorithm to generate the rough fracture surface and used a mechanistic model to calculate the distribution of aperture during shearing. Cardona et al. created synthetic fractal surfaces using the power law, contact mechanics, and kinematic constraints to explore the evolution of aperture distribution during shear displacement and normal loading. Song et al. [23] performed direct shear tests to study the description of permeability anisotropy-based joint shear deformation of natural sandstone replicated by artificial materials. Chen et al. [19] carried out direct shear test conditions to study the influence of anisotropy of roughness on the shear failure mechanism of fracture surfaces under constant normal load (CNL). However, the anisotropic of rough-walled rock fracture during shearing has not been studied in the previous studies.

In the present study, four standard sandstone samples were extracted from the original sandstone sample. A rough-walled fracture exists in the original sandstone sample. To consider the anisotropic properties of rough-walled rock fractures, intersection angles between the axis along the height direction of cylindrical standard sandstone samples and the axis along the height direction of the original sample are different. The hydraulic properties of each standard sandstone sample were tested under different shear displacements and confining pressures.

2. Experimental Setup

2.1. Original Sample Preparation and Surface Roughness Measurement. The porosity and permeability of the matrix of sandstones used in this study are 20.3% and 2.71×10^{-8} m^2. The original rock block was cut and polished to a rectangular sample. The size of the rectangular block is 200 mm in length, 100 mm in width, and 100 mm in height. Brazilian splitting test was performed to manufacture tensile fracture along the center of the rectangular block in the height direction.

Three-dimensional characterization and digital reconstruction of fracture surface topography were carried out using a high-precision noncontact 3D laser scanner as shown in Figure 1(a). The 3D laser scanner has a horizontal (x, y) scanning accuracy of $\pm20\,\mu$m and a vertical (z) scanning accuracy of $\pm10\,\mu$m.

The scanning interval in both x and y directions is set to 0.5 mm, and the 3D reconstruction results are shown in Figure 1(b). According to the recommended method of the International Society for Rock Mechanics and Engineering [25], a series of equidistant two-dimensional (xz) sections are extracted every 2 mm along the y direction on the three-dimensional rough fracture surface to quantitatively characterize the roughness coefficient of the three-dimensional fracture surface. Referring to the experiences of previous scholars [26], the point spacing of 1 mm is selected along the y direction for the two-dimensional section and the joint roughness coefficient (JRC) is calculated according to the following formulas:

$$Z_2 = \left[\frac{1}{M} \sum \left(\frac{z_{i-1} - z_i}{x_{i-1} - x_i}\right)^2\right]^{1/2}, \tag{1}$$

$$\mathrm{JRC} = 32.2 + 32.47 \lg Z_2, \tag{2}$$

where M is the number of sample points selected along the y direction, x_i and z_i are the coordinates of sample points on the two-dimensional contour.

As shown in Figure 2(a), the fracture surface height of fracture surface goes through three stages, including uphill, hill, and downhill, along the y direction (shear direction). The fluctuation height distribution frequency of the scanning point obeys the typical Gaussian distribution. The minimum value of fracture surface height is 3.08 mm, and the maximum value of fracture surface height is 12.43 mm. The mean value of fracture surface height is 7.91 mm, and the standard deviation (StDev) is 1.92 mm. The distribution of JRC values of two-dimensional (xz) sections, which are extracted every 2 mm along the y direction on the three-dimensional rough fracture surface, is shown in Figure 2(b).

2.2. Sample Extraction. The sample preparation process can be divided into three stages. First, cylindrical samples were extracted from the original rectangular sandstone using different sampling methods as shown in Figures 3(a)–3(c). The preparation process of the original rectangular sandstone sample and the geometrical characteristics of the artificial fracture surface in the specimen have been described in Section 2.1. In the extraction process, each drilling angle between the axis along the height direction of cylindrical
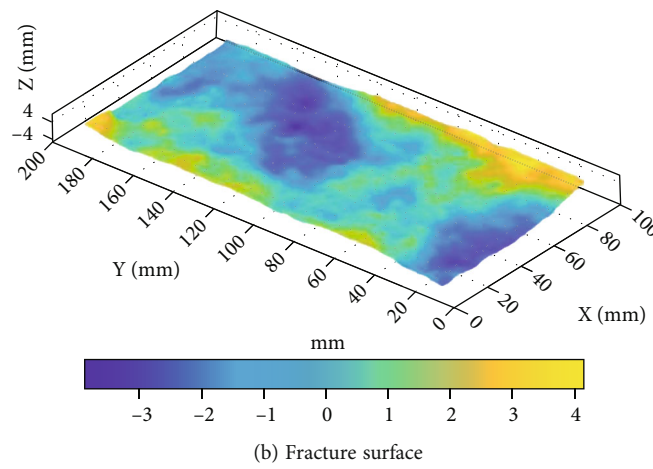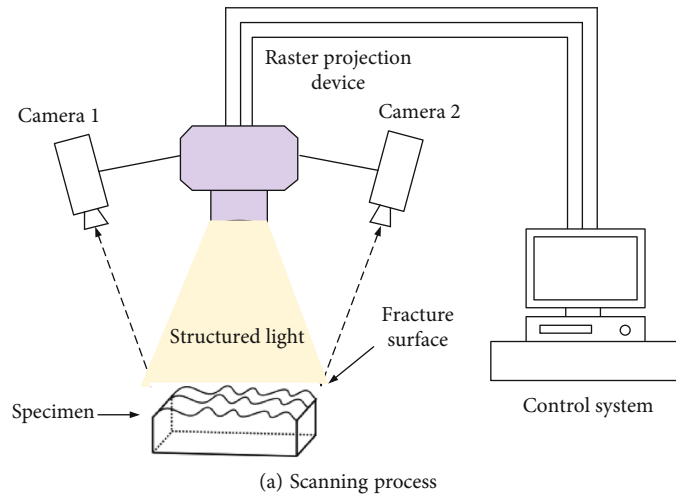
(a) Scanning process

(b) Fracture surface

Figure 1: Roughness acquisition.

(a) The frequency of fracture surface height

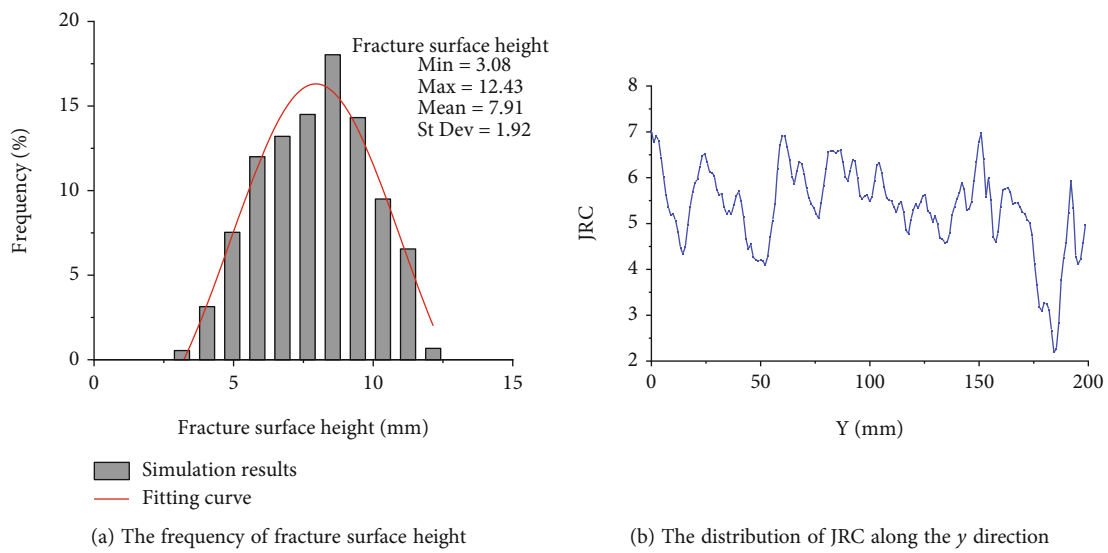(b) The distribution of JRC along the y direction

Figure 2: The geometric characteristics of the rough fracture surface.

sandstone samples and the artificial fracture of the original sample is different. The four drilling angles are 0°, 45°, 90°, and 135°. Samples drilled at 0° and 90° are samples with a diameter of 50 mm and a height of 100 mm, as shown in Figure 3(d). The sizes of samples drilled at 45° and 135° are 50 mm in diameter and 70 mm in height. Since the drilling
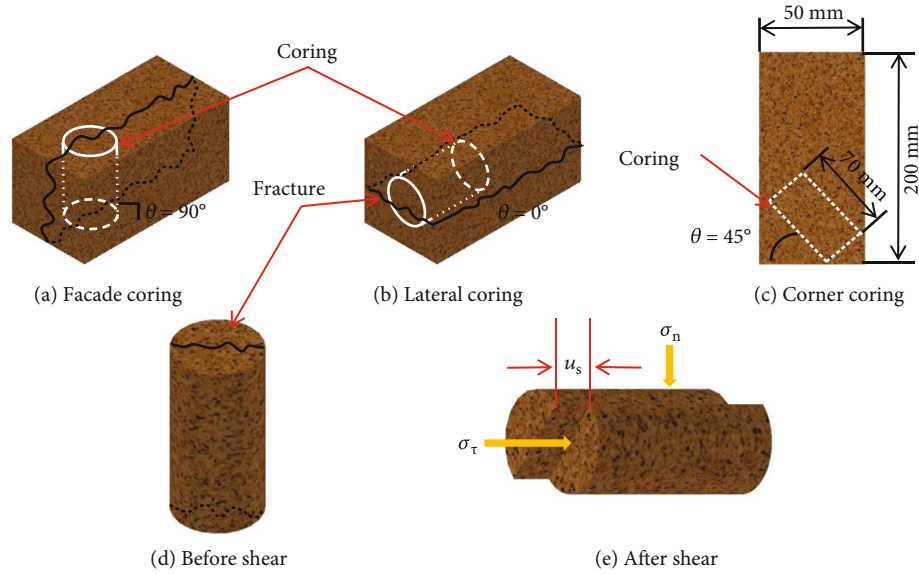
FIGURE 3: Sample preparation: (a–c) sandstone with varying coring methods, (d) cored sandstone sample, and (e) extraction process during shearing.
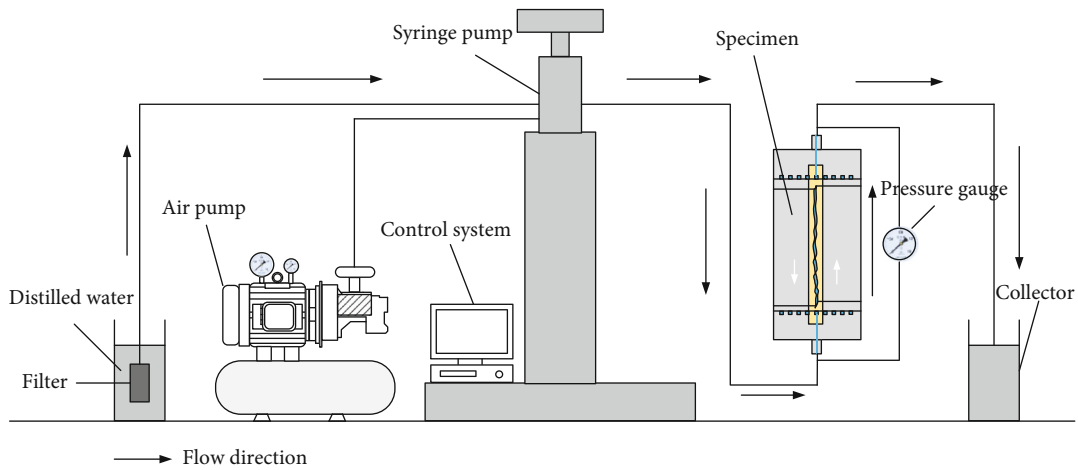

FIGURE 4: Multifunctional seepage testing apparatus.

angles of 45° and 135° are symmetrical, only 45° is shown in Figure 3(c).

To investigate the influence of the shear displacement on the hydraulic properties of cylindrical samples, the position of the rock blocks on both sides of the fracture is adjusted according to the shear displacement (u_s) as shown in Figure 3(e). The shear displacement is set to be 2 mm, 3 mm, and 4 mm, respectively. In order to ensure the stability of the sample during the seepage test, rigid gaskets are added at both ends of the cylindrical samples.

2.3. Testing Procedure. The seepage tests under different flow velocities and confining pressures (σ_n) were carried out using the multifunctional seepage testing system as shown in Figure 4. The test system is mainly consisted of the water injection device, sample holder, and data acquisition device. The water injection device includes a filter, air pump, syringe pump, and control system. The data acquisition device includes a pressure gauge and collector. The sample holder can apply confining pressure on the cylindrical sample. The accuracy of confining pressure was 0.1 MPa, and the accuracy of the volumetric flow velocity was 0.01 m/s. For each sample, different flow velocities ranging from 0 m/s to 13 m/s were designed. For a given flow velocity, different confining pressures (σ_n) were applied. During the test process, the fractured sample was first put into the holder after being equipped with a rubber sleeve. Then, different confining pressures, including 1.5 MPa, 2.5 MPa, and 3.5 MPa, were applied on the fractured sample. Applying axial stress can effectively protect the rubber sleeve from being damaged by the confining pressure. For a given flow velocity and confining pressure, the difference in pressure gradient (∇P) between the inlet and the outlet of the samples and flow rate (Q) was recorded in real-time using the automatic data acquisition system.
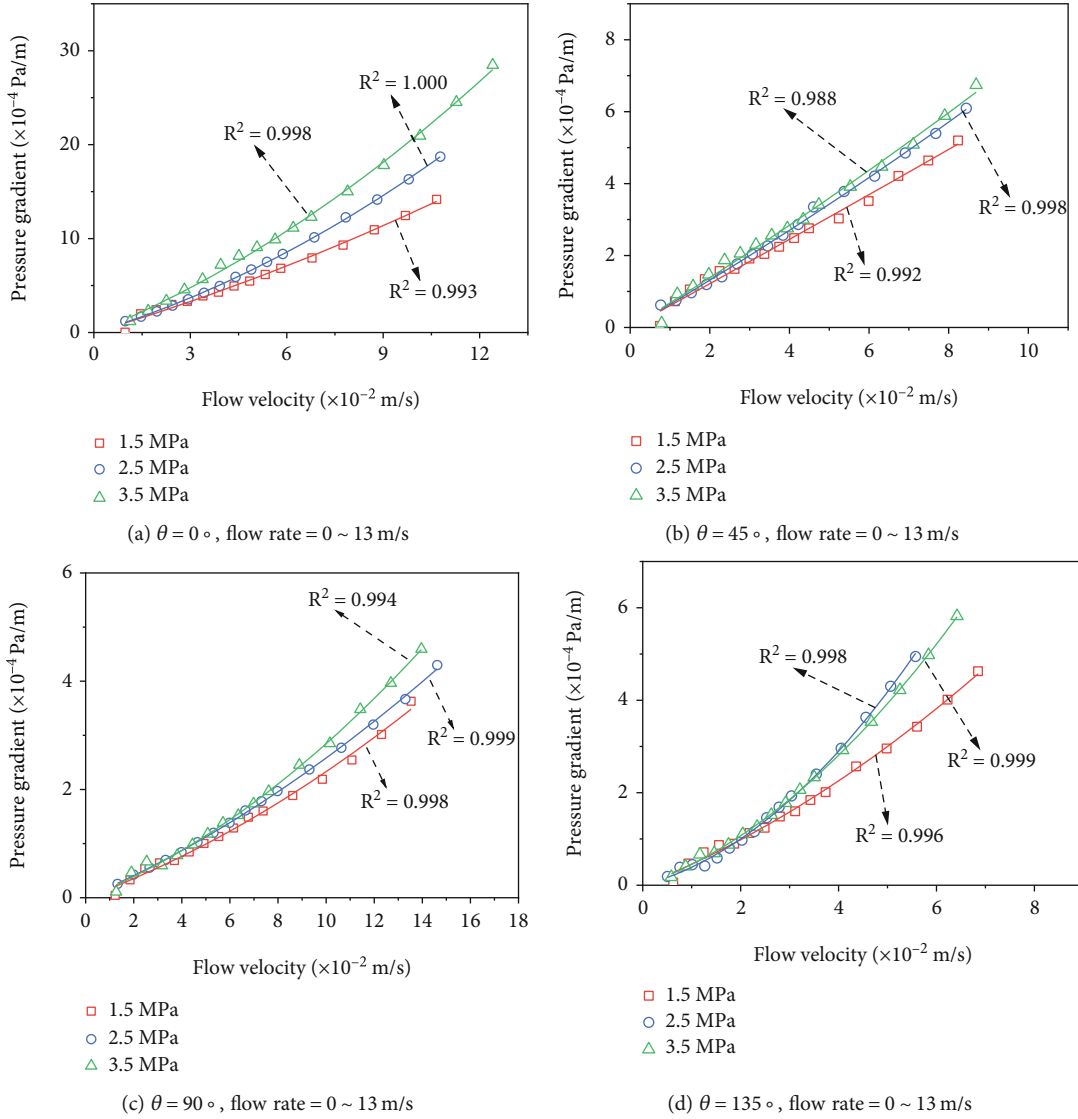
(a) $\theta = 0°$, flow rate $= 0 \sim 13$ m/s

(b) $\theta = 45°$, flow rate $= 0 \sim 13$ m/s

(c) $\theta = 90°$, flow rate $= 0 \sim 13$ m/s

(d) $\theta = 135°$, flow rate $= 0 \sim 13$ m/s

FIGURE 5: Evolution of pressure gradient under different confining pressures σ_n and drilling angle θ with varying flow velocity from 0 to 13 m/s.

The Reynolds number Re is defined as the ratio of inertial forces to the viscous forces and can be formulated as follows [27, 28]:

$$\mathrm{Re} = \frac{\rho Q}{\mu w}, \tag{3}$$

where ρ is the fluid density, w is the fracture width, and μ is the dynamic viscosity.

The apparent transmissivity T is a commonly used parameter to describe the flow state of fluids. If the flow follows a Darcy-type law, it is found that T is independent of Re:

$$T = \frac{E^3}{12} = -\frac{\mu Q}{w \nabla P} = -\frac{\mu Q}{w(\mathrm{AQ})} = T_0 = \mathrm{constant}, \tag{4}$$

where E is the hydraulic aperture, A is the linear coefficient, and T_0 is the intrinsic transmissivity.

As the flow rate increases, doubling the pressure drop does not produce a double flow rate, which is known as the nonlinear flow. In this regime, the apparent transmissivity is given by the following:

$$T = -\frac{\mu Q}{w \nabla P} = -\frac{\mu Q}{w(\mathrm{AQ} + \mathrm{B}Q^2)}, \tag{5}$$

where B is the nonlinear coefficient.

For a fixed flow channel, a nonlinear relationship between flow rate and pressure drop exists for a strong inertial regime, especially at a relatively high flow rate. The normalized transmissivity (T/T_0) is defined as the ratio of apparent transmissivity (T) to intrinsic transmissivity (T_0), which is used to characterize the transition of fluid from
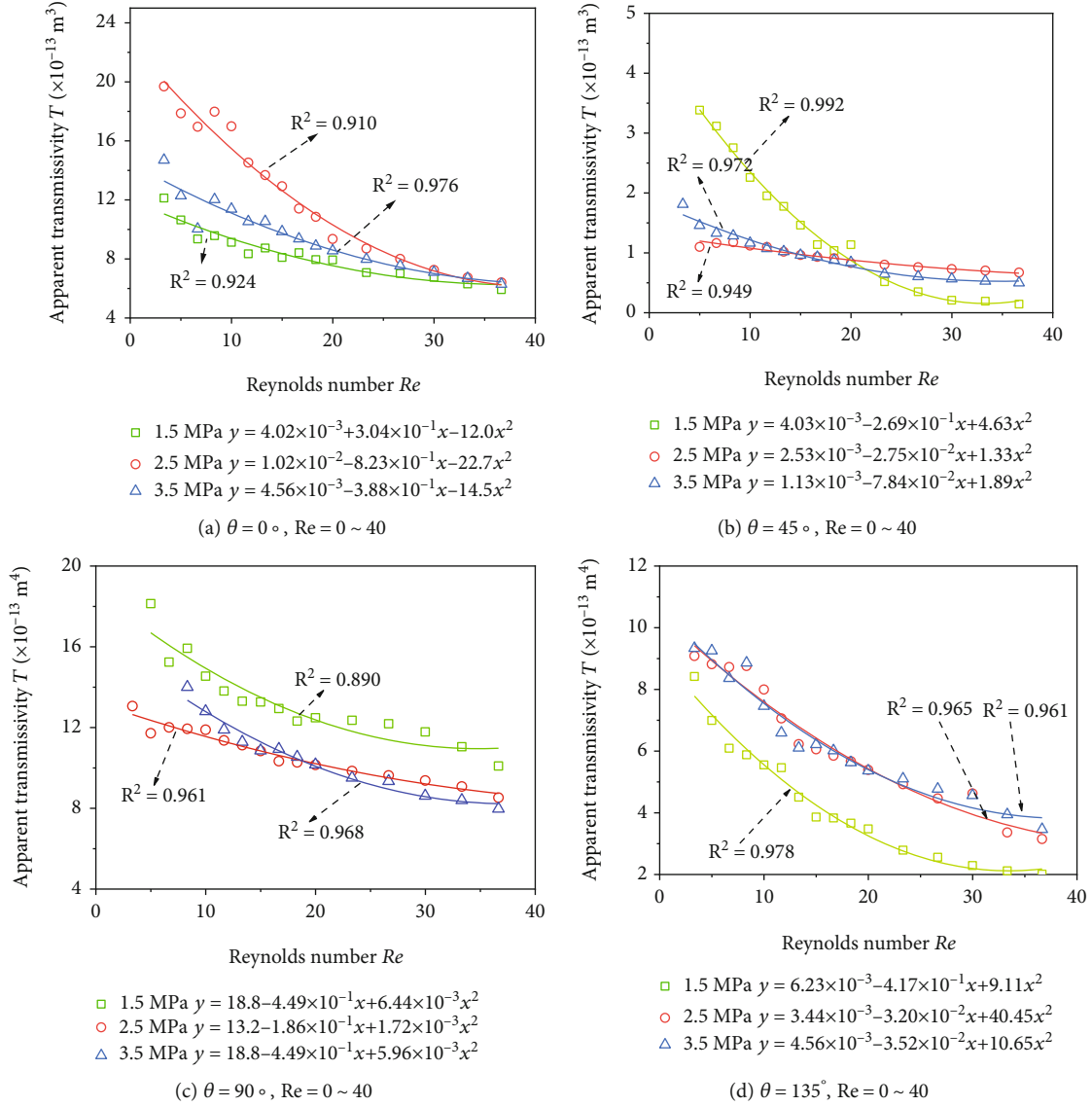
FIGURE 6: Evolution of apparent transmissivity T under different confining pressures σ_n and drilling angle θ with varying Reynolds' number Re from 0 to 40.

linear regimes to nonlinear regimes. Therefore, the rate of T to T_0 is calculated by the following:

$$\frac{T}{T_0} = \frac{-\mu Q/w\left(AQ + BQ^2\right)}{-\mu Q/w(AQ)} = \frac{AQ}{AQ + BQ^2}. \quad (6)$$

When the fluid flow is in a linear state, T_0 corresponds to the value of T. When the nonlinear term (BQ^2) accounts for 10% of the pressure drop, that is, $T/T_0 = 0.9$, it is considered as the critical condition for the fluid to change from linear to nonlinear [29–31].

3. Results and Discussion

3.1. Effect of Extraction Angle of Standard Samples on Hydraulic Properties.
Figure 5 shows the relationships between $-\nabla P$ and Q for water flow through the fracture.

The flow velocity is in the range of 0–13 m/s, and the corresponding pressure gradient is in the ranges of $0 - 27.9 \times 10^{-4}$, $0 - 6.7 \times 10^{-4}$, $0 - 4.5 \times 10^{-4}$, and $0 - 5.8 \times 10^{-4}$ Pa/m, for $\theta = 0°$, 45°, 90°, and 135°, respectively. For a certain θ, as σ_n increases, the pressure gradient shows an increasing trend. The best-fit regression analyses were conducted on the experimental data using the Forchheimer equation and were plotted as the solid lines. The values of residual squared R^2 for all cases are larger than 0.99, which indicates that the experimental values agree well with the fitting curves.

$T/T_0 = 0.9$ has the same physical meaning that the non-linear term (BQ^2) contributes to 10% of the pressure drop, in which the current Re is Re_c. As shown in Figure 6, with the increment of Re, the T presented a reduction trend, and the decreasing rate gradually weakened, which confirmed the existence of flow nonlinearity in fractures. Figure 7 shows that Re_c is in the ranges of 5.4-13.4, 18.8-32.1, 3.92-7.47,
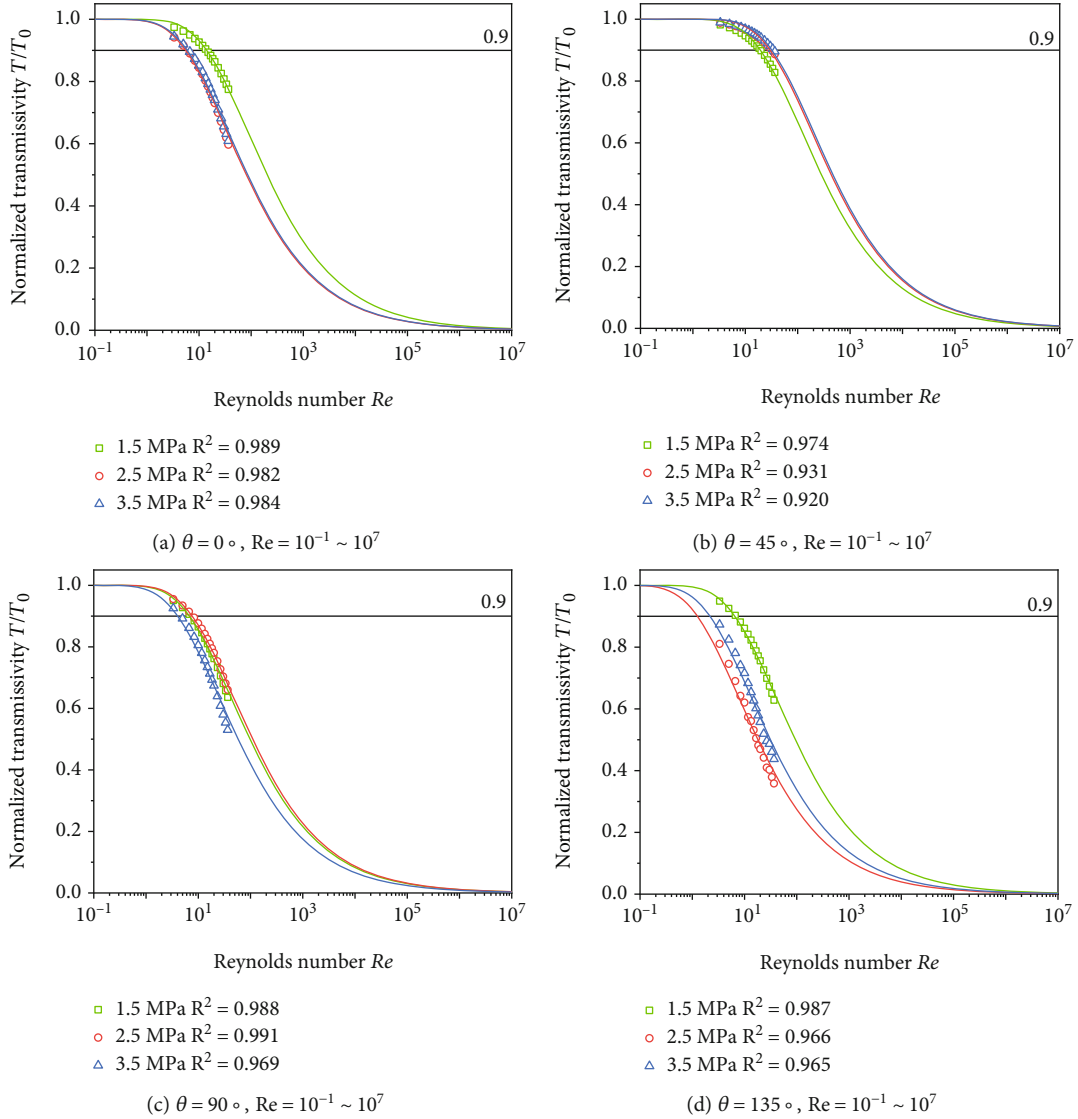
FIGURE 7: Evolution of the normalized transmissivity T/T_0 under confining pressures σ_n and drilling angle θ with varying Reynolds' number Re.

and 1.16-6.69 for $\theta = 0 \circ$, 45°, 90° and 135°, respectively. Generally, T/T_0 remains constant at 1.0 for Re = 0.01 – 1 with $\theta = 0 \circ$, 45° and 90°, and it exhibits a remarkable decrease when Re > 1. When $\theta = 135°$, T/T_0 remains constant at 1.0 for Re = 0.01 – 0.1, and it exhibits a remarkable decrease when Re > 0.1.

For fluid flow through fractured media, the normalized transmissivity T/T_0 has also been applied to estimate the nonlinear flow regime [32]. The variations in T/T_0 against J can be expressed as follows:

$$\frac{T}{T_0} = 1 - \exp\left(-\alpha J^{-0.45}\right). \tag{7}$$

The values of T/T_0 were calculated and plotted in terms of J as shown in Figure 8. As J increases, T/T_0 shows a downward trend. The variations in T/T_0 with J can be divided into three stages. When J is small, T/T_0 approxi-

mately holds a constant value of 1.0; thus, the fluid flow is within the linear regime. Then, with the continuous increase of J, T/T_0 decreases, and the reduction rate first increases and then decreases. Based on Equation (7), when $T/T_0 = 0.9$, J_c can be calculated and is in the ranges of 2.26-5.12, 4.27–5.71, 0.09–0.66 for $\theta = 0 \circ$, 45°, 90°, 135°, respectively.

3.2. Effect of Shear Displacement on Hydraulic Properties. The dislocation of rock will change the void space in the fracture. As a result, the shear displacement will cause the change of the fracture seepage characteristics, such as T and T/T_0. Different shear displacements are carried out for the fractures with different cutting angles, and the evolution characteristics of T/T_0 are shown in Figure 9. With the increase of hydraulic gradient, T/T_0 gradually decreases, which means that the proportion of nonlinear flow is increasing. This is because with the increase in hydraulic gradient, the inertial flow of the fracture increases, and the sample is more enable to enter the nonlinear flow stage.
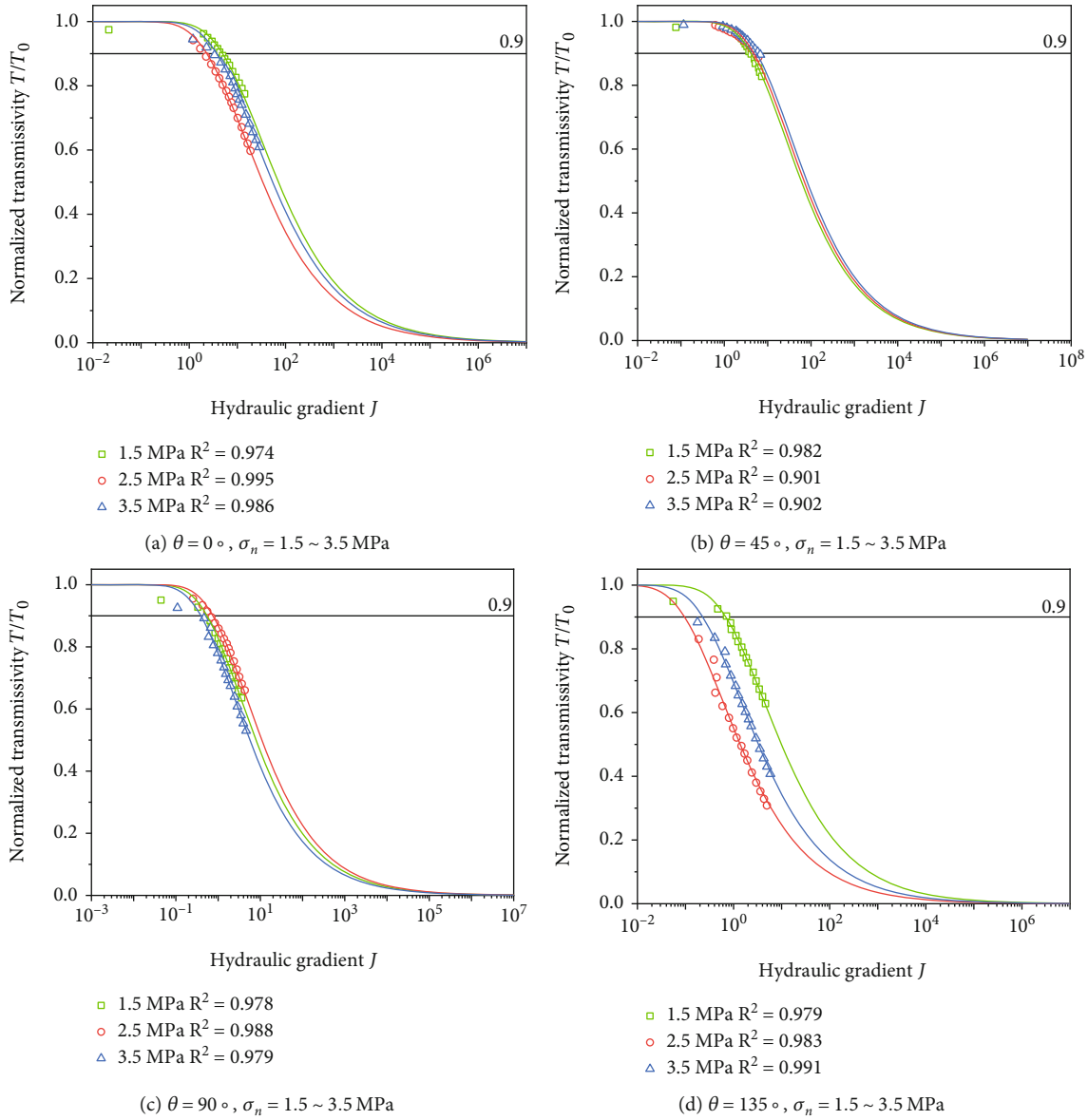
(a) $\theta = 0°$, $\sigma_n = 1.5 \sim 3.5$ MPa

(b) $\theta = 45°$, $\sigma_n = 1.5 \sim 3.5$ MPa

(c) $\theta = 90°$, $\sigma_n = 1.5 \sim 3.5$ MPa

(d) $\theta = 135°$, $\sigma_n = 1.5 \sim 3.5$ MPa

FIGURE 8: Relation between normalized transmissivity T/T_0 and hydraulic gradient J when confining pressure $\sigma_n = 1.5$ MPa, 2.5 MPa, and 3.5 MPa.

We take $T/T_0 = 0.9$ as a reference value, which means the proportion of nonlinear flow will account for 10%, and the fluid will change from a linear flow regime to a nonlinear flow regime. When $u_s = 2$ mm, the J of the samples with 0° and 45° angles is 4.73 and 3.85 when reaching $T/T_0 = 0.9$, which is significantly larger than that of the samples with 90° and 135° angles ($J = 0.53$ and 0.71). This is because with the increment of the cutting angle, the corresponding fractures are rougher when the shear displacement is 2 mm, and there are more contacts in the fracture. The flow rate Q required for the fluid to enter the nonlinear flow stage is smaller; therefore, the required critical hydraulic gradient J_c is smaller. It is worth noting that as shear advances, the J_c of the fracture with a cutting angle of 90° becomes larger when $T/T_0 = 0.9$, which indicates that the fracture is obviously affected by shear displacement. This results in a larger

void space and less contacts in the fracture and makes it more difficult for the fractures to enter the nonlinear flow stage. Therefore, a larger J is required to get the critical value. However, for other fractures such as the fracture with a cutting angle of 0°, the J_c decreases with the increase of shear displacement, which indicates that the seepage characteristics of fractured rock mass under different cutting angles are obviously different.

Figure 10 shows the variation characteristics of T/T_0 with Reynolds' coefficient of fractures with different cutting angles under different shear displacements. The Re_c of the fracture with a cutting angle of 90° is different from that of other samples. When the $u_s = 2$ mm, 3 mm, and 4 mm, the corresponding Re_c is 6.52, 28.73, and 32.1. This shows that with the increase of shear displacement, the void space is larger, and Re_c is larger. In contrast, for other fractures such
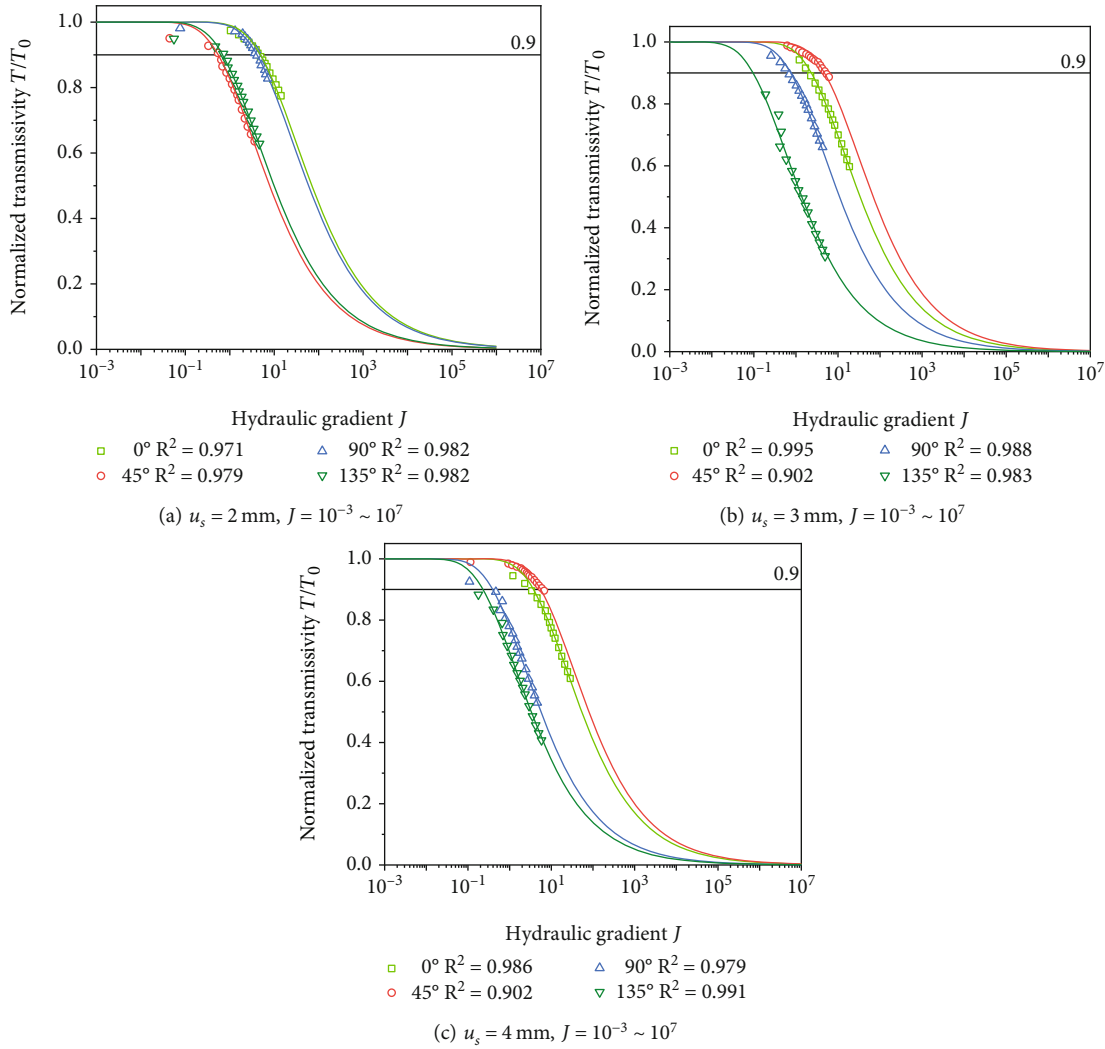
FIGURE 9: Evolution of normalized transmissivity T/T_0 under confining pressures and angles with varying hydraulic gradient J and shear displacement u_s.

as the fracture with a cutting angle of 0°, when $u_s = 2$ mm, 3 mm, and 4 mm, the corresponding Re_c continuously decreases, which is different from the fracture with 90°. This shows that J and Re_c of the fracture that changes from linear flow regime to nonlinear flow regime under different cutting angles have different variation characteristics, depending on the geometric characteristics of fracture surfaces.

3.3. Effect of Coring Directions with Confining Pressures.
Figure 11(a) compares Re_c contours for samples of different drilling angles under different confining pressures. The variations in Re_c along different drilling angles are significantly obvious. It is fully explained that the Re_c of the same rough fracture surface are also anisotropic. When the confining pressure is large (e.g., 2.5 MPa and 3.5 MPa), the difference between Re_c of samples with different drilling angles is small. This shows that when the confining pressure is large, the effect of anisotropy on Re_c is much greater than that of confining pressure. Figure 11(b) compares J_c contours for samples of different drilling angles under different confining pressures. When the confining pressure is small (e.g.,

1.5 MPa and 2.5 MPa), the difference between J_c of samples with different drill angles is relatively small. This shows that when the confining pressure is small, the effect of anisotropy on J_c is much greater than that of confining pressure.

Figure 12(a) compares Re_c contours for samples of different drilling angles with different u_s. The variations in Re_c along different drilling angles are significantly obvious. It is proved that the Re_c of the same rough fracture surface are anisotropic on the other hand. When u_s is large (e.g., 3 mm and 4 mm), the difference between Re_c of samples with different drilling angles is relatively small. This shows that when u_s is large, the effect of anisotropy on Re_c is much greater than that of u_s. Figure 12(b) compares J_c contours for samples of different drilling angles under different u_s. The variations in J_c along different drilling angles are significantly obvious. It is further indicated that the J_c of the same rough fracture surface is anisotropic. Regardless of the value of u_s, the difference between J_c is very obvious. When the confining pressure is small (e.g., 1.5 MPa and 2.5 MPa), the difference between J_c of samples with different drill angles is relatively small. This shows that when the

(a) $u_s = 2$ mm, Re $= 10^{-1} \sim 10^7$

(b) $u_s = 3$ mm, Re $= 10^{-1} \sim 10^7$
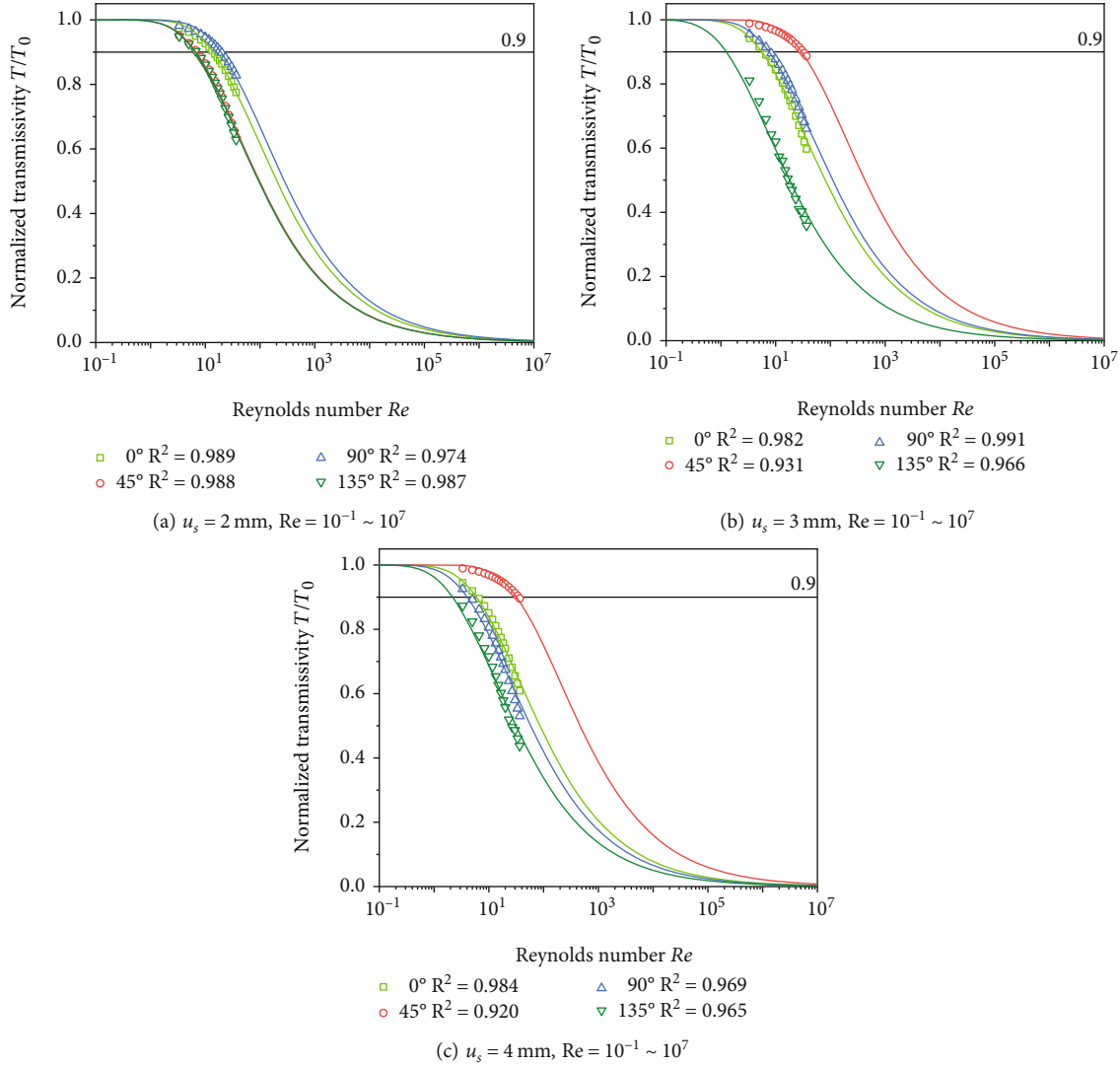

(c) $u_s = 4$ mm, Re $= 10^{-1} \sim 10^7$

FIGURE 10: Evolution of normalized transmissivity T/T_0 under confining pressures and angles with varying Reynolds' number Re and shear displacement u_s.

confining pressure is small, the effect of anisotropy on J_c is much greater than that of confining pressure. So, anisotropy is important for the hydraulic properties of fractured rock masses.

4. Conclusions

To consider the anisotropic properties of rough-walled rock fracture, four cylindrical sandstone samples were extracted from the original rectangular sample with a rough-walled fracture. A series of seepage tests were carried out to investigate the hydraulic properties of cylindrical sandstone samples with different shear displacements (u_s) under different confining pressures (σ_n).

The results show that the apparent transmissivity (T) decreases with the increment of Reynolds' number (Re), and the decreasing rate gradually weakened, which confirmed the existence of flow nonlinearity in fractures. As the hydraulic gradient (J) increases, the normalized trans-

missivity (T/T_0) decreases. The variations in T/T_0 with J can be divided into three stages. When J is small, T/T_0 approximately holds a constant value of 1.0; thus, the fluid flow is within the linear regime. Then, with the continuous increase of J, T/T_0 decreases, and the reduction rate first increases and then decreases. When $u_s = 2$ mm, 3 mm, and 4 mm, the values of critical Reynolds' number (Re$_c$) are 6.52, 28.73, and 32.1, respectively. This shows that with the increase in u_s, the void space is larger, and Re$_c$ is larger. In contrast, for other fractures such as the fracture with a cutting angle of 0°, when $u_s = 2$ mm, 3 mm, and 4 mm, the Re$_c$ continuously decreases, which is different with the fracture with 90°. This shows that J and Re$_c$ of the fracture that changes from linear flow regime to nonlinear flow regime under different cutting angles have different variation characteristics, depending on the geometric characteristics of the fracture surface. The variations in Re$_c$ and J along different drilling angles are significantly obvious. It is fully explained that the Re$_c$ and J of the same rough

(a) Re_c distributions with different σ_n
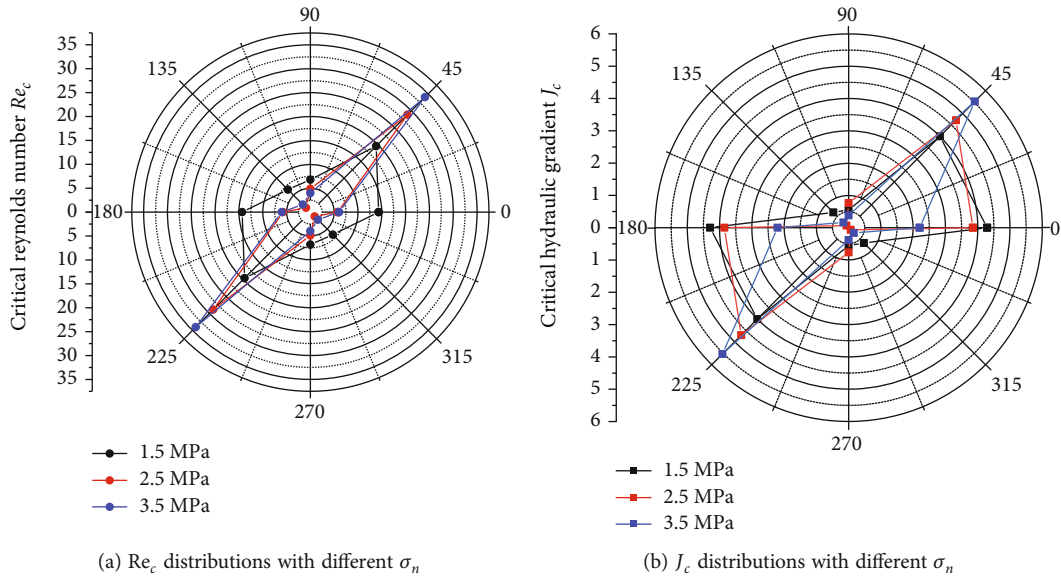
(b) J_c distributions with different σ_n

FIGURE 11: The distributions of critical Reynolds' number Re_c and critical hydraulic gradient J_c in different directions with different confining pressures σ_n.

(a) Re_c distributions with different u_s
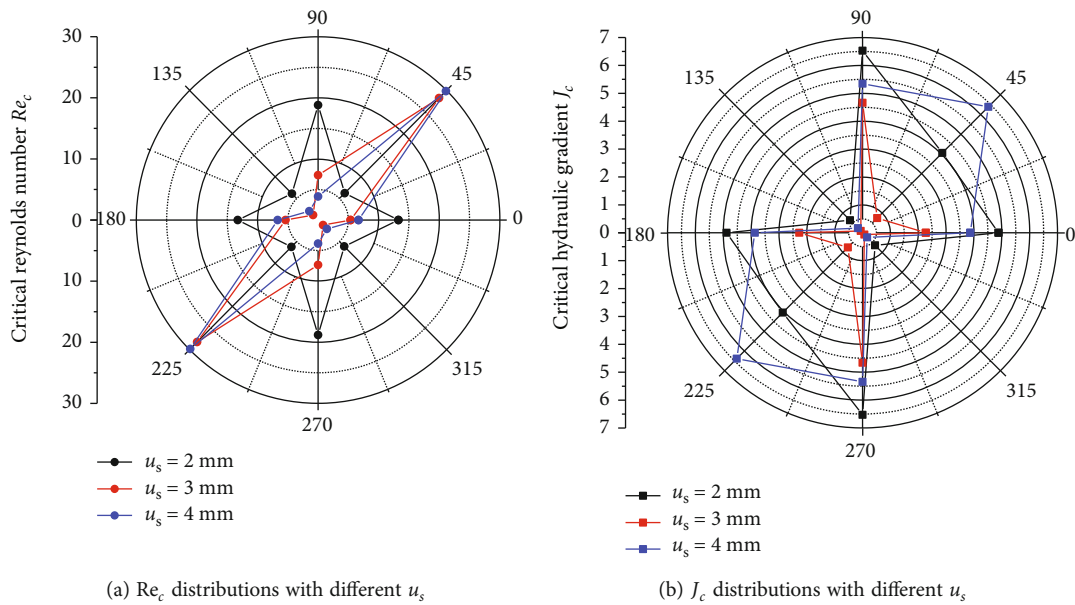
(b) J_c distributions with different u_s

FIGURE 12: The distributions of critical Reynolds' number Re_c and critical hydraulic gradient J_c in different directions with different shear displacements u_s.

fracture surface are also anisotropic. When the confining pressure is large (e.g., 2.5 MPa and 3.5 MPa), the difference between Re_c of samples with different drilling angles is small. This shows that when the confining pressure is large, the effect of anisotropy on Re_c is much greater than that of confining pressure.

The permeability of fractures is several times larger than that of the matrix, and the connected fractures/fracture networks provide the dominant flow paths for fluid through hard or crystalline rocks during the shearing process. In the future work, we will investigate the mechanisms of opening/closure of fractures induced by shear/normal stresses

and clarify the separate roles of fractures and matrix on permeability during shearing.

Data Availability

The data can be obtained by contacting the author after the manuscript is accepted.

Conflicts of Interest

The authors declare that they have no conflict of interest.

Acknowledgments

References

[1] A. Baghbanan and L. Jing, "Hydraulic properties of fractured rock masses with correlated fracture length and aperture," *International Journal of Rock Mechanics and Mining Sciences*, vol. 44, no. 5, pp. 704–719, 2007.

[2] R. Liu, B. Li, and Y. Jiang, "A fractal model based on a new governing equation of fluid flow in fractures for characterizing hydraulic properties of rock fracture networks," *Computers and Geotechnics*, vol. 75, pp. 57–68, 2016.

[3] K. B. Min, L. Jing, and O. Stephansson, "Determining the equivalent permeability tensor for fractured rock masses using a stochastic REV approach: method and application to the field data from Sellafield, UK," *Hydrogeology Journal*, vol. 12, no. 5, pp. 497–510, 2004.

[4] C. Müller, S. Siegesmund, and P. Blum, "Evaluation of the representative elementary volume (REV) of a fractured geothermal sandstone reservoir," *Environmental Earth Sciences*, vol. 61, no. 8, pp. 1713–1724, 2010.

[5] M. Wang, P. Kulatilake, J. Um, and J. Narvaiz, "Estimation of REV size and three-dimensional hydraulic conductivity tensor for a fractured rock mass through a single well packer test and discrete fracture fluid flow modeling," *International Journal of Rock Mechanics and Mining Sciences*, vol. 39, no. 7, pp. 887–904, 2002.

[6] J. Song, M. Dong, S. Koltuk, H. Hu, L. Zhang, and R. Azzam, "Hydro-mechanically coupled finite-element analysis of the stability of a fractured-rock slope using the equivalent continuum approach: a case study of planned reservoir banks in Blaubeuren, Germany," *Hydrogeology Journal*, vol. 26, no. 3, pp. 803–817, 2018.

[7] W. Xu, Y. Zhang, X. Li et al., "Extraction and statistics of discontinuity orientation and trace length from typical fractured rock mass: a case study of the Xinchang underground research laboratory site, China," *Engineering Geology*, vol. 269, article 105553, 2020.

[8] L. Jing, "A review of techniques, advances and outstanding issues in numerical modelling for rock mechanics and rock engineering," *International Journal of Rock Mechanics and Mining Sciences*, vol. 40, no. 3, pp. 283–353, 2003.

[9] Y. Chen, S. Hu, R. Hu, and C. Zhou, "Estimating hydraulic conductivity of fractured rocks from high-pressure packer tests with an Izbash's law-based empirical model," *Water Resources Research*, vol. 51, no. 4, pp. 2096–2118, 2015.

[10] Y. He, Z. Zhu, W. Lu, Y. Tian, X. Xie, and S. Wang, "Experimental study on seepage anisotropy of a hexagonal columnar jointed rock mass," *Shock and Vibration*, vol. 2021, Article ID 6661741, 15 pages, 2021.

[11] N. Huang, Y. Jiang, B. Li, and R. Liu, "A numerical method for simulating fluid flow through 3-D fracture networks," *Journal of Natural Gas Science and Engineering*, vol. 33, pp. 1271–1281, 2016.

[12] B. Kong and S. Chen, "Numerical simulation of fluid flow and sensitivity analysis in rough-wall fractures," *Journal of Petroleum Science and Engineering*, vol. 168, pp. 546–561, 2018.

[13] A. Lavrov, "Comparison of symmetric and asymmetric schemes with arithmetic and harmonic averaging for fracture flow on Cartesian grids," *Transport in Porous Media*, vol. 142, no. 3, pp. 585–597, 2022.

[14] L. Zou, L. Jing, and V. Cvetkovic, "Roughness decomposition and nonlinear fluid flow in a single rock fracture," *International Journal of Rock Mechanics and Mining Sciences*, vol. 75, pp. 102–118, 2015.

[15] Y. B. Gong, M. Sedghi, and M. Piri, "Two-phase relative permeability of rough-walled fractures: a dynamic pore-scale modeling of the effects of aperture geometry," *Water Resources Research*, vol. 57, no. 12, article e2021WR030104, 2021.

[16] Y. B. Gong, M. Sedghi, and M. Piri, "Dynamic pore-scale modeling of residual trapping following imbibition in a rough-walled fracture," *Transport in Porous Media*, vol. 140, no. 1, pp. 143–179, 2021.

[17] M. Ahmadi, A. D. Taleghani, and C. M. Sayers, "The effects of roughness and offset on fracture compliance ratio," *Geophysical Journal International*, vol. 205, no. 1, pp. 454–463, 2016.

[18] A. Cardona, T. Finkbeiner, and J. C. Santamarina, "Natural rock fractures: from aperture to fluid flow," *Rock Mechanics and Rock Engineering*, vol. 54, no. 11, pp. 5827–5844, 2021.

[19] F. Chen, H. Yu, Y. Yang, and D. Wu, "Influences of roughness sampling interval and anisotropy on shear failure mechanism of rock joint surface," *Energies*, vol. 14, no. 21, p. 6902, 2021.

[20] P. S. Lang, A. Paluszny, M. Nejati, and R. W. Zimmerman, "Relationship between the orientation of maximum permeability and intermediate principal stress in fractured rocks," *Water Resources Research*, vol. 54, no. 11, pp. 8734–8755, 2018.

[21] R. Liu, M. He, N. Huang, Y. Jiang, and L. Yu, "Three-dimensional double-rough-walled modeling of fluid flow through self- affine shear fractures," *Journal of Rock Mechanics and Geotechnical Engineering*, vol. 12, no. 1, pp. 41–49, 2020.

[22] R. Liu, N. Huang, Y. Jiang, H. Jing, and L. Yu, "A numerical study of shear-induced evolutions of geometric and hydraulic properties of self-affine rough-walled rock fractures," *International Journal of Rock Mechanics and Mining Sciences*, vol. 127, article 104211, 2020.

[23] Y. Song, B. Liu, H. Liu, X. Shi, D. Ren, and M. Yu, "A method to obtain artificial sandstone joint specimens for the description of permeability anisotropy-based joint shear deformation," *Geomechanics and Geophysics for Geo-Energy and Geo-Resources*, vol. 7, no. 2, pp. 1–19, 2021.

[24] H. Kim, J. Inoue, and H. Horii, "Flow analysis of jointed rock masses based on excavation-induced transmissivity change of rough joints," *International Journal of Rock Mechanics and Mining Sciences*, vol. 41, pp. 959–974, 2004.

[25] ISRM, "Rock characterization, testing and monitoring-ISRM suggested methods," in *Suggested methods for the quantitative description of discontinuities in rock masses*, E. T. Brown, Ed., pp. 3–52, E. T. Brown, Pergamon, 1981.

[26] N. Huang, R. Liu, Y. Jiang, B. Li, and L. Yu, "Effects of fracture surface roughness and shear displacement on geometrical and hydraulic properties of three-dimensional crossed rock fracture models," *Advances in Water Resources*, vol. 113, pp. 30–41, 2018.

[27] R. W. Zimmerman, A. Al-Yaarubi, C. C. Pain, and C. A. Grattoni, "Non-linear regimes of fluid flow in rock fractures," *International Journal of Rock Mechanics and Mining Sciences*, vol. 41, no. 3, pp. 163–169, 2004.

[28] J. Q. Zhou, S. H. Hu, S. Fang, Y. F. Chen, and C. B. Zhou, "Nonlinear flow behavior at low Reynolds numbers through rough-walled fractures subjected to normal compressive loading," *International Journal of Rock Mechanics and Mining Sciences*, vol. 80, pp. 202–218, 2015.

[29] G. Rong, J. Yang, L. Cheng, and C. Zhou, "Laboratory investigation of nonlinear flow characteristics in rough fractures during shear process," *Journal of Hydrology*, vol. 541, pp. 1385–1394, 2016.

[30] Z. Zhang and J. Nemcik, "Fluid flow regimes and nonlinear flow characteristics in deformable rock fractures," *Journal of Hydrology*, vol. 477, no. 1, pp. 139–151, 2013.

[31] Q. Yin, R. C. Liu, H. W. Jing, H. J. Su, L. Y. Yu, and L. X. He, "Experimental study of nonlinear flow behaviors through fractured rock samples after high-temperature exposure," *Rock Mechanics and Rock Engineering*, vol. 52, no. 9, pp. 2963–2983, 2019.

[32] Q. Yin, H. W. Jing, G. W. Ma, H. J. Su, and R. C. Liu, "Investigating the roles of included angle and loading condition on the critical hydraulic gradient of real rock fracture networks," *Rock Mechanics and Rock Engineering*, vol. 51, no. 10, pp. 3167–3177, 2018.